



**HAL**  
open science

## Quasi-static drainage in a network of nanoslits of non-uniform depth designed by grayscale laser lithography

Antoine Naillon, Hajar Massadi, Rémi Courson, Jean Bekhit, Lucie F Seveno, Pierre-François Calmon, Marc Prat, Pierre Joseph

► **To cite this version:**

Antoine Naillon, Hajar Massadi, Rémi Courson, Jean Bekhit, Lucie F Seveno, et al.. Quasi-static drainage in a network of nanoslits of non-uniform depth designed by grayscale laser lithography. *Microfluidics and Nanofluidics*, 2017, 21 (8), pp.131. 10.1007/s10404-017-1970-z . hal-01566417

**HAL Id: hal-01566417**

**<https://laas.hal.science/hal-01566417v1>**

Submitted on 21 Jul 2017

**HAL** is a multi-disciplinary open access archive for the deposit and dissemination of scientific research documents, whether they are published or not. The documents may come from teaching and research institutions in France or abroad, or from public or private research centers.

L'archive ouverte pluridisciplinaire **HAL**, est destinée au dépôt et à la diffusion de documents scientifiques de niveau recherche, publiés ou non, émanant des établissements d'enseignement et de recherche français ou étrangers, des laboratoires publics ou privés.

# Quasi-static drainage in a network of nanoslits of non uniform depth designed by grayscale laser lithography

A. Naillon<sup>1,2</sup>, H. Massadi<sup>2</sup>, R. Courson<sup>3</sup>, J. Bekhit<sup>2</sup>, L. Seveno<sup>2</sup>, P.F. Calmon<sup>2</sup>, M. Prat<sup>1</sup>, P. Joseph<sup>2\*</sup>

<sup>1</sup>INPT, UPS, IMFT (Institut de Mécanique des Fluides de Toulouse), Université de Toulouse, Allée Camille Soula, F-31400 Toulouse, France

<sup>1</sup>CNRS, IMFT, F-31400 Toulouse, France

<sup>2</sup>LAAS-CNRS, Université de Toulouse, CNRS, Toulouse, France

<sup>3</sup>Kloe SA, 1068 Rue de la Vieille Poste, F-34000 Montpellier, France

**Abstract:** A method is reported to fabricate silicon-glass nanofluidic chips with non-uniform channel depths in the range 20-500 nm and micrometer resolution in width. The process is based on grayscale laser lithography to structure photoresist in 2.5 dimensions in a single step, followed by a reactive ion etching to transfer the resist depth profile into silicon. It can be easily integrated in a complete process flow chart. The method is used to fabricate a network of interconnected slits of non-uniform depth, a geometry mimicking a nanoporous medium. The network is then used to perform a pressure step controlled drainage experiment, i.e. the immiscible displacement of a wetting fluid (liquid water) by a non-wetting one (nitrogen). The drainage patterns are analyzed by comparison with simulations based on the invasion percolation algorithm. The results indicate that slow drainage in the considered nanofluidic system well corresponds to the classical capillary fingering regime.

**Key words:** nanofluidics, porous media, drainage, nanofabrication, grayscale lithography, varying depth

## 1. Introduction

Immiscible two-phase flows in porous media are encountered in many fields of practical interest, such as petroleum engineering, ground water hydrology or chemical engineering to name only a few. The literature on the subject is vast and this is still a very active research field, e.g. (Cottin et al. 2010; He et al. 2015; Lee et al. 2015; Jung et al. 2016) and references therein. Consider the process where a fluid totally occupied the pore space initially and is displaced by the injection of another fluid. When the displacing fluid is the wetting phase the process is called imbibition whereas drainage corresponds to the displacement of a wetting fluid by a non-wetting fluid (Dullien 1992). In what follows, we are interested in the drainage process. The drainage theory is well established since the eighties, namely since the work of (Lenormand et al. 1988). Considering the situations where gravity effects can be neglected, they showed that the process was essentially controlled by the viscosity ratio of the two fluids and the competition between the viscous and capillary forces. Three main asymptotic regimes, referred to as the capillary fingering regime, the DLA regime and the stable displacement regime, were identified. The stable displacement and DLA

---

\* Corresponding author: pjoseph@laas.fr, +33 (0)5 61 33 63 60

regimes, where DLA stands for Diffusion-Limited Aggregation (Witten and Sander 1981), correspond to regimes where capillary effects are negligible compared to viscous effects whereas the capillary fingering regime corresponds to a displacement exclusively controlled by capillary effects. This led to a drainage diagram, generally referred to as Lenormand's diagram, summarizing the main patterns expected in drainage.

These results were notably obtained from a series of experiments performed in quasi two-dimensional model media consisting in square networks of interconnected channels of randomly variable hydraulic diameter. The channel sizes were large, on the order of a few hundred microns. There is, however, no doubt that Lenormand's diagram also applied in the micrometric range, with pores between 1  $\mu\text{m}$  and 100  $\mu\text{m}$  in size, e.g. (Zhang et al. 2011; Jung et al. 2016).

The situation is less clear as regards the porous materials with pores in the nanometric range, which corresponds in this paper to pore sizes between about 10 nm and a few hundred nanometers.

This is an important class to which porous materials such as concrete, mortar, clays, clay rocks, etc belong. The classical approach in engineering is actually to assume that the models used for computing two phase flows in the micrometric range, namely the generalized Darcy's law, (Dullien 1992), still applies in the nanometric range. Returning to Lenormand's approach, this implicitly amounts to assuming that the situation with pore sizes in the nanometric range is not significantly different from the one prevailing in systems with bigger pore sizes. However, to the best of our knowledge, this assumption has never been confirmed from visualization experiments on model porous media analogous to the ones performed in the micrometric and submillimeter ranges. This is so because fabricating model systems with pores in the nanometric range is much less straightforward than for bigger sizes, and also because the pattern visualization is also much more difficult when the pore sizes are on the order of the light wave lengths in the visible or even smaller. Also, recent experimental studies on a simple geometry such as single straight channels or slits in the nanometric range indicate differences with the results valid in micrometric channels. The spontaneous imbibition process is reported to be slower than predicted by the classical Washburn's law (Washburn 1921), e.g. (Chauvet et al. 2012; Vincent et al. 2016) and references therein. As reported in (Duan et al. 2012), evaporation can be faster than in micrometric channels owing to the impact of bubble formation and trapping. Although these processes are not drainage, they are examples of two-phase processes indicating that the situation in nanometric systems can show differences with the one in systems with bigger pores. It can be noted, however, that the drainage experiments in a system of nanoslits in parallel reported in (Wu et al. 2014) do not lead to identify significant differences in the flow patterns compared to those observed in conventional-sized tubes. However, this study is limited to flows in straight channels of uniform depth. While investigating flows in individual straight channels is a natural first step, studying the flows in systems of interconnected channels of variable depth is highly desirable so as to consider pore spaces with geometrical properties, such as a distribution in the pore size and the existence of interconnections, closer to the ones existing in real porous media.

In this context, the objective is first to develop a model nanoporous system enabling one to study nanoscale flows in a system of interconnected channels, while permitting visualization using optical microscopy. These two apparently contradictory aspects can be met fabricating a network of interconnected nanoslits of depth in the 10-100 nm range and width in the micrometric range. This last dimension permits a direct visualization of the two fluid phases in the slits as shown for instance for systems of nanoslits in parallel in (Chauvet et al. 2012) or (Wu et al. 2014). Fabricating a network of interconnected slits is however a challenge since standard fabrication techniques

typically lead to network of uniform depth, e.g. (He et al. 2015) and references therein. Since capillary effects are mostly controlled by the smallest dimension of the slit cross section, here the slits depth and not their width, it is crucial that the slits depth varies from one slit to the other in the network. This important aspect is achieved by adapting grayscale lithography to nanofluidics to get 2.5D nanofluidic networks. Then the network of interconnected slits is used to perform a quasi-static drainage experiment in order to explore whether the nano-confinement leads to significant differences compared to the classical description presented in (Lenormand et al. 1988). The experiments are analyzed by comparison with numerical simulations based on the classical invasion percolation algorithm (Wilkinson and Willemsen 1983), which is well adapted to model the capillary fingering regime of Lenormand's diagram, at least again in systems with pore size greater than 1 micron. We focus on the quasi-static regime because this is the conventional regime to compute macroscopic properties of interest, such as the capillary pressure curve or the relative permeabilities, using pore network models, e.g. (Blunt et al. 2002). However, the nano porous device presented in what follows could be used in future works for studying the other regimes of Lenormand's diagram.

## **2. Development of a direct writing technique to fabricate varying-depth nano-slits.**

### **2.1. Different approaches to fabricate nano-slits with complex depth profile**

Standard nanofabrication techniques are intrinsically in two dimensions (2D) because common processes are based on the deposition of thin layers (photoresist or structural materials like metals) followed by their patterning and/or etching (Madou 2011). Consequently, fluidic channels can now be fabricated down to few nanometers sizes by many methods (Duan et al. 2013), but most of them are in 2D. However, 3D relief opens the path to model media with topologies more representative of a real porous media. More generally, in term of micro and nanofluidic application, it makes available functionalities not accessible in 2D as the entropic manipulation of DNA (Stavis et al. 2012) or the sorting and characterization of nanoparticles (Stavis et al. 2010).

In this perspective, efforts have been made recently to get nanochannels in 3D. The first class of 3D nanofabrication techniques is based on point-by-point direct writing of each 3D point (voxels) by a very narrow focalization beam; the volume of each written voxel being in the sub- $\mu\text{m}^3$  range. The absence of physical mask makes this approach rapidly reconfigurable and thus good for prototyping. For example, femtosecond laser is often used in manufacturing due to its ability to reach high energy density with limited heating (Sugioka and Cheng 2014). It permits fabricating directly submicrometric channels via optical breakdown (Ke et al. 2005), 50 nm nanochannels buried in glass thanks to non-linear beam-substrate interaction (Liao et al. 2013), nanotunnels in metal inter-layer (Zhang et al. 2013). Femtosecond lasers are also involved in two-photon polymerization (Sugioka and Cheng 2014) to pattern objects in the 10-100 nm range (Li et al. 2009; Selimis et al. 2015). Another direct writing technique is based on the use of electron-beam (e-beam) or ions. The same type of buried nanochannels as in (Liao et al. 2013) have been achieved by Azimi *et al.* combining ion beam irradiation, electrochemical anodization and high temperature oxidation (Azimi et al. 2014).

As a compromise between fully 3D and 2D fabrication, the second group of direct writing methods is based on grayscale lithography (GL), often denoted 2.5D. Its principle is to modulate spatially the exposure dose applied to the resist (**Fig. 1a**), which permits constructing non-uniform-depth

structures in one step. Erdmanis *et al.* and Kim *et al.* have demonstrated grayscale patterning with e-beam lithography (Kim *et al.* 2007; Erdmanis and Tittonen 2014).

The previous approaches however involve point-by-point writing of nano-voxels or nano-pixels which are very time consuming and expensive for wafer-scale processing. To avoid long processing time, two variants of 2.5D methods have been proposed: gray tone masks and Digital-Micro-mirror Device (DMD®) (Totsu *et al.* 2006; Rammohan *et al.* 2011; Zhong *et al.* 2014). In the former, 2.5D fabrication is achieved by using a physical mask whose transparency is not uniform. The variation of optical density can be produced by an array of small diffractive elements (Stavis *et al.* 2009) or a continuous transparency variation (Wu *et al.* 2002). It has the advantage to be compatible with simple lithography. However, it suffers from the need of one mask per design (mask cost and fabrication time). Furthermore, its use was only implemented for large structures. In the only example of this method for nanofluidics, Stavis *et al.* have fabricated channels by gray tone mask with depth in the few hundreds of nanometers range (Stavis *et al.* 2009) but with a demonstrated lateral resolution no better than about 100  $\mu\text{m}$ . In Digital-Micro-mirror Device (DMD®) technique, a UV light is reflected on an array of mirrors which can simultaneously insolate different pixels on the substrate. However the pixel size is around 10  $\mu\text{m}$  (Totsu *et al.* 2006), and to the best of our knowledge, it was not implemented for nanofluidic applications.

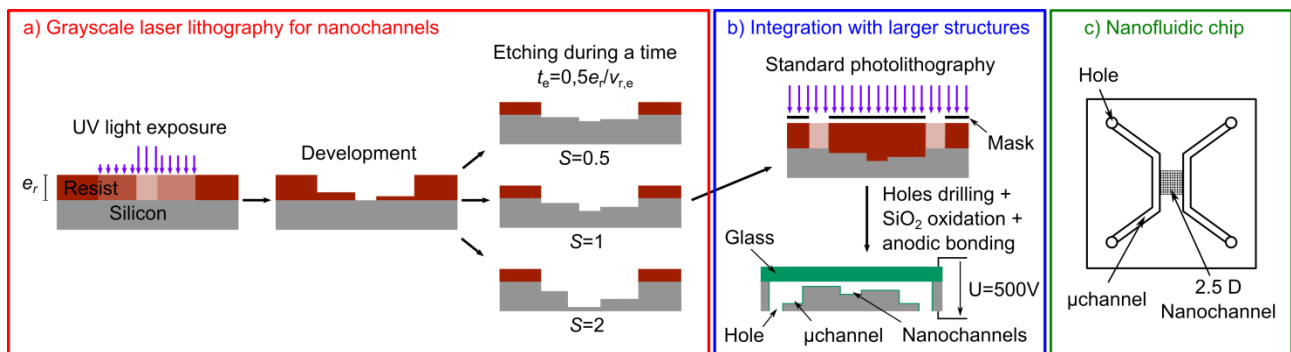


**Fig. 1** Flow chart of the fabrication process. a) Principle of grayscale laser lithography to fabricate varying depth nanochannels in one step. b) Nanochannels are integrated in the nanofluidic chips with standard fabrication steps. c) Scheme of the final nanofluidic chip.

As we discuss in the introduction, many nanofluidic studies need channels with nanometers depth but can take advantage of few micrometers width if the mechanism involved is controlled by the smallest size. Indeed, micrometer width allows a high throughput analysis and/or it is implemented to use standard optical microscope for observation. In our case, the capillary effects are controlled by the smallest size which imposes meniscus curvature (see section 3.3 and Eq.(1) below). None of the approaches presented above is fully suited to realize non-uniform-depth nanochannels with micrometer lateral size in a single step. For that purpose, we develop a process, based on grayscale laser direct writing lithography (GLDWL) which fully meets all of those criteria. This maskless technique is ideal for prototyping of nanofluidic experiments and fits easily in a standard process flow. In context of microoptics, GLDWL was reported 20 years ago in the work of Gale *et al.* to fabricate micro-optical planar elements in positive photoresist (Gale *et al.* 1994). Surprisingly, to the best of our knowledge, it has not been adapted to nanofluidics yet. Here, GLDWL is optimized to integrate nanochannels with depths from 20 nm to 500 nm obtained in a single step, with good

lateral resolution (around 2  $\mu\text{m}$ ) and low writing time (a few minutes to get a full channel network, less than 3 hours for a complete four-inch wafer).

In the following sections, we first describe the optimized process and then present the nanofluidic structures fabricated in 2.5 dimensions.

## 2.2 Fabrication process

Nanofluidic chips are realized following the process flowchart presented in *Fig 1*. First, nanochannels with varying depths are structured in a 1.06  $\mu\text{m}$  layer of positive photoresist AZ ECI 3012 (Microchemicals GmbH), commonly used for binary lithography which needs  $\sim\mu\text{m}$  spatial resolution. The photoresist is spin coated on a silicon wafer at 3600 rpm with an acceleration of 5000 rpm/s. The silicon wafer is previously exposed to 800 W  $\text{O}_2$  plasma during 5 min to ensure its cleanliness and to favor the photoresist adhesion.

UV light exposure is performed with the laser direct writing machine Dilase 750 (Kloé SA). On this machine, the laser remains fixed and the sample is placed on a stage moving at a velocity  $v$ . A 405 nm laser beam is collimated and focused by a 10x Olympus UPlanFL N objective with a numerical aperture of 0.3. Three focused spot diameters  $D$  can be used: 0.5, 2 and 20  $\mu\text{m}$ , on three different optics lines. Moreover, the laser power,  $P$ , is modulated by a factor,  $m$ , from 10% to 100% of the initial laser power ( $P = mP_0$  with  $P_0 = 100$  mW). Filters with a transmittance  $T$  can be added on the light path to attenuate the initial laser power. Thus, the local exposure dose  $E$ , defined as the amount of light energy received by the photoresist per surface unit, is controlled by these five local parameters and linked by the relation:  $E \sim \frac{mTP_0 D}{\pi D^2 v}$ . This qualitative relation depicts that the exposure dose corresponds to the time during which a point is exposed to a given laser power density. The relation is only semi-quantitative because it does not take into account the Gaussian shape of the beam. For our study, we use the spot diameter  $D = 2$   $\mu\text{m}$  because it is the best compromise to achieve the desired lateral resolution while limiting the writing time. Structures with lateral dimensions larger than spot diameter are designed with successive adjacent beam passages every 1  $\mu\text{m}$ . It is the maximal distance (thus the minimum writing time) that still ensures a homogeneous exposure on the surface (see *Fig SI.2*, SI).

Then, exposed resist is developed in MF CD 26 solution. In case of binary lithography, resists as AZ ECI 3012 are optimized to have a binary comportment, with a high contrast. This means that under a threshold of exposure dose, the resist development rate tends to zero and is constant and high above it. On the contrary, to perform GL, it is interesting to use a photoresist with low contrast and low selectivity. The ideal case for GL is to have a linear relationship between the exposure dose and the resist development rate (MicroChemicals GmbH 2013). To this end, the soft bake process of the AZ ECI 3012 is optimized with respect to standard conditions (95°C, 2 min), by setting its temperature to 125°C during 5 min. This reinforced thermal treatment decomposes a significant part of the photoactive compounds, which slows and smoothens the relationship between development rate and exposure dose (*Fig. 2a*). This provides a good control of the removed resist thickness. In addition, development rate becomes independent of development time, contributing to reproducibility and robustness of the process.

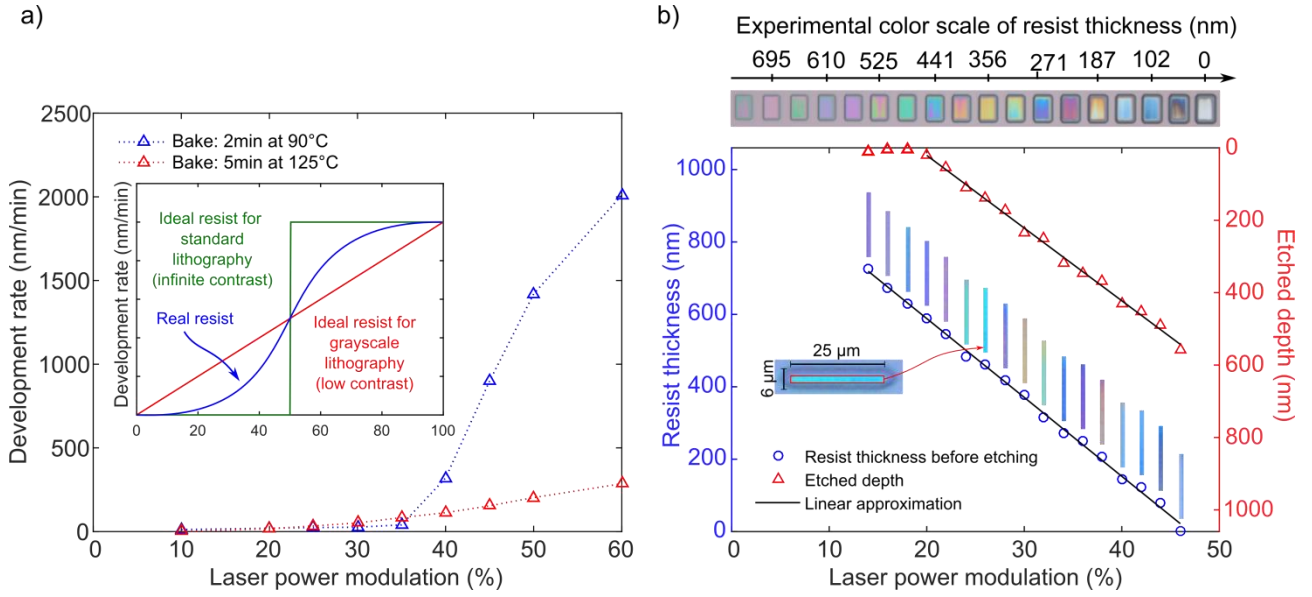


**Fig. 2** a) Optimization of the soft bake step to obtain a linear relation between the development rate and the exposure dose with a low development rate. Process parameters:  $P_0=100$  mW,  $T=3\%$ ,  $D = 2$   $\mu\text{m}$ ,  $v = 5$  mm/s. In the inset, ideal compartment of grayscale or standard photoresist. b) On the top: optical image of  $20 \times 30$   $\mu\text{m}^2$  rectangles after resist development, showing Newton color scale. Main graph: resist thickness after 30 s of development (blue circle, left axis) and depth after 2 min of etching (red triangle, right axis) against laser power modulation of  $6 \times 25$   $\mu\text{m}^2$  rectangles.

After exposure and development, 2.5D structures are patterned in the resist (blue points in **Fig. 2b**). Then, they are transferred into silicon by reactive ion etching (RIE). The remaining resist acts as a retardant to start the silicon etching. The two key parameters of this step are the silicon etching rate,  $v_{Si,e}$  and the resist etching rate,  $v_{r,e}$ . Their ratio defines the etching selectivity:  $S = v_{Si,e}/v_{r,e}$ . Knowing these etching rates, the remaining resist thickness,  $e_r$ , and the etching time,  $t_e$ , the etched silicon depth can be written as:  $d_{Si} = v_{Si,e}t_e - Se_r$ . As illustrated in **Fig. 1a**, a value of  $S$  lower than one reduces the resist thickness variation transferred in silicon whereas a value higher than 1 increases it. Usually in binary lithography, RIE is designed to have the highest  $S$  as possible. It permits etching a high depth of silicon with a thin layer of resist to achieve a good lateral resolution. Here, the process is optimized to have selectivity around 1: in this way, the resist structures are identically reported in silicon. We also demonstrate tuning of selectivity by playing with etching parameters. This is discussed in SI 2b.

Before designing complex 2.5D structures,  $30 \mu\text{m} \times 20 \mu\text{m}$  and straight channels with constant but different depths demonstrate the mastery of the process. The only control parameter is the laser power modulation to change the exposure dose (writing velocity  $v=0.4$  mm/s,  $T=0.3\%$ , and development time 30 s). **Fig. 2b** shows that laser power modulation ( $m$ ) linearly controls the remaining resist thickness before etching (in blue), as well as the silicon etched depth for fixed etching conditions (in red). Nanochannels with constant, chosen depths in the range 0-600 nm are thus obtained. The remaining resist thickness can be quickly checked with optical observation: white light interference creates an experimental Newton color scale. The resolution of this

measurement is better than 40 nm that is why it was used for decades in different contexts (Lin and Sullivan 1972). This is very useful for large scale and quick characterization of devices. For example, an intentional defect is circled in green in **Fig. 3** to illustrate that defects can be rapidly identified by color inspection.

In order to get a functional device, the integration of non-uniform depth nanochannels in the nanofluidic chips is done with standard methods (**Fig. 1b**). Microchannels of  $300 \times 5 \mu\text{m}^2$  cross section are etched by RIE after binary photolithography in order to supply fluid to the nanochannels. Then access holes are sand blasted in silicon. The chip is capped with a glass wafer by anodic bonding. Before the bonding, a 50 nm thick layer of silicon oxide is thermally grown homogeneously on the silicon surface. It provides a symmetrical wetting condition in channels increasing the hydrophilicity of silicon. It also prevents nanochannel's collapse, by reducing the electrostatic forces during the bonding (Shih 2004; Duan and Majumdar 2010).

In order to summarize the ability of our process, two different structures are presented in **Fig. 3** of GLDWL: slope channels and step channels. In other word, it is feasible to design in one step channels with continuous varying depth, or channels with a depth varying by step. These, 2.5D structures can be seen as elementary components to design more complex geometries as model to porous media. A feature of our technique is that the Gaussian intensity profile of the beam is transferred to the resist, creating non-sharp lateral frontiers. This effect is important only on a distance of the order of the beam diameter  $D$ . Nanochannels with lateral dimensions no larger than a few  $D$  have a cross-section shape closer to a parabola than to a rectangle. The lateral cross section of channels shown in **Fig. 3** is parabolic and varies between  $6 \mu\text{m} \times 250 \text{ nm}$  and  $8.1 \mu\text{m} \times 400 \text{ nm}$ . Larger structures are much less affected:  $20 \times 30 \mu\text{m}^2$  rectangles on the top of **Fig. 2b** have a flat and homogeneous surface.

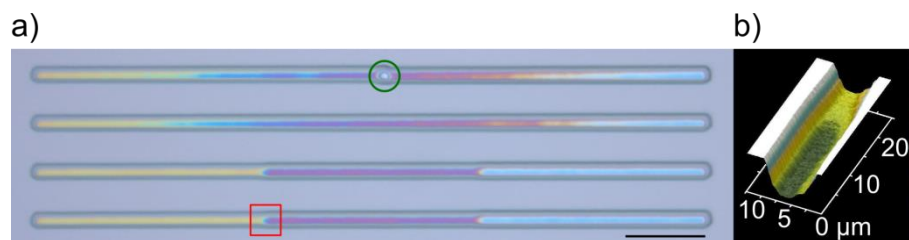


**Fig. 3** Picture of two slope channels (top) and two channels composed of three steps (bottom), shown in true colors before etching. Black scale bar is  $50 \mu\text{m}$ . The green circle highlights an intentional defect. b) AFM picture of a step corresponding to the red rectangular zone in a). The color scale represents a depth from 0 (white) to 400 nm (black).

In terms of writing time, a  $400 \mu\text{m}$  long straight channel presented in **Fig. 3** is written in less than 1 min (a transversal line of the stair channel is written in only 0.025s); The pore network presented in **Fig. 4** is written in around 9 min.

The range of achievable depths is 0 to  $1 \mu\text{m}$  with a control over depth better than 10 nm (see standard deviation in **Fig. 2b**). The lateral minimum width can be reduced down to  $2 \mu\text{m}$  using only 1 beam passage. Large structures can also be designed using adjacent beam passages or a larger beam, which decreases the writing time. The rapidity of the process, its spatial resolution, and its versatility to design all kind of complex 2.5 nanostructures is well suited for the prototype phase

and application in nanofluidics. In the following, we demonstrate the use of our device for fluid flow experiments in complex geometries mimicking a nanoporous medium.

### 3. Quasi-static drainage

#### 3.1 Experimental nano-slit networks

Nanostructures with non-uniform depths fabricated as reported in the previous sections are used to perform drainage experiments. As illustrated in **Fig. 4**, a  $400\ \mu\text{m} \times 400\ \mu\text{m}$  quasi two-dimensional square network is used. It is composed of  $14 \times 16$  pores interconnected by  $15 \times 15$  bonds (a bond is the nano-slit connecting two neighbor pores). The depth of a bond is constant all along its length. The depth of each bond is assigned by randomly drawing a depth from six values (in practice, we assign a laser power value which will give a resin thickness developed after lithography and then a depth to the channel as a result of the silicon etching). We limit ourselves to six values of depth in order to facilitate the control of the robustness of the manufacturing protocol (we can quickly check that two bonds that we want to be of identical depth are indeed of identical depth). The depth of all the pores is the same and is greater than that of the deepest bond. This is obtained by strong laser exposure of pores.

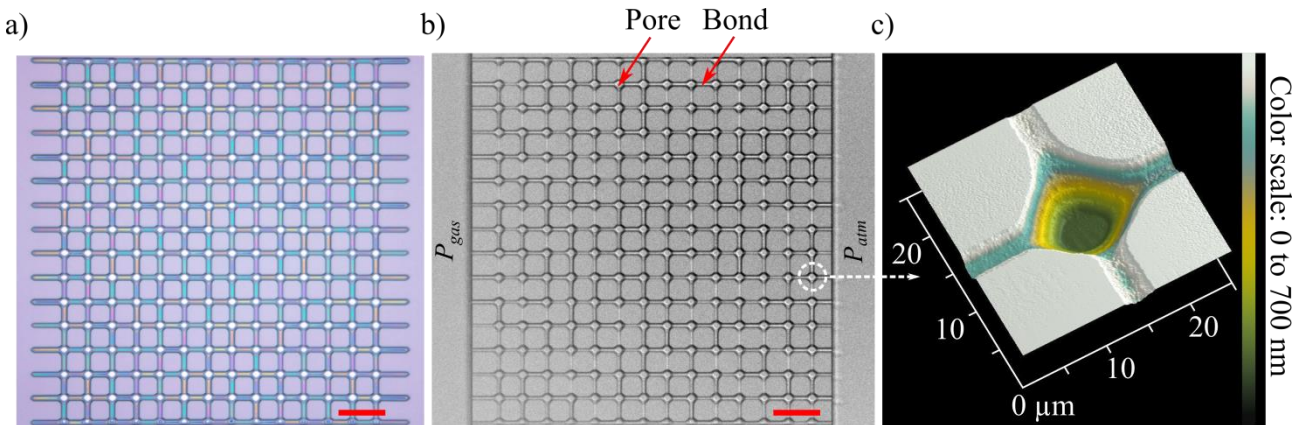


**Fig. 4** Illustration of network with nano-slits of variable depth. a) Image acquired before etching, after laser lithography and development. Each color corresponds to a different photoresist thickness (true colors). b) The same device once finished (after silicon etching and bonding to glass). The length scale (red bar) represents  $50\ \mu\text{m}$ . c) AFM picture around the pore circled in b).

Five devices have been developed (Naillon 2016). Each device has been used several times injecting the displacing fluid on the left side of network and vice versa (so as to obtain two liquid-gas distributions for each device). The repeatability was excellent. Basically, the same pattern is obtained when the experiment is repeated with the same device for the same experimental conditions. Also, the experimental result main features are similar for all tested devices and selected injection side. Since similar results are obtained with the five devices, we only present the results obtained with the device corresponding to the slit depths in the smaller range, namely varying between 0 and 225 nm as indicated in Table 1. As can be seen, two depth ranges are indicated in Table 1, one for the vertical bonds and one for the horizontal bonds. Indeed, the slit depth range of this device is slightly shifted between the vertical slits and the horizontal slits due to a technological choice. For full wafer processing, we slightly defocused the laser beam which writes the structures in order to spread its power over a larger surface. It smoothen uneven etching and exposure that

would result from non-horizontality and non-planarity of the substrate. Lateral resolution is still of the order  $2\ \mu\text{m}$  as demonstrated in *Fig. 4*. This defocusing is actually asymmetrical and makes the beam oval rather than circular. The dose of light energy that a point receives then depends on the writing direction, vertical or horizontal. When we indicate a lower bound of depth 0, there is still a thin layer of resist on the silicon at these locations even after etching corresponding to low laser exposure,.

Bond depth (nm)	h: 30 – 69 – 108 – 147 – 186 – 225 v: 0 – 0 – 22 – 61 – 100 – 140
Capillary pressure range (bar)	h: 6.5 – 48.5 v: 10.4 – $\infty$

**Table 1** Experimental nano-slit network geometrical properties; h denotes the horizontal bonds and v the vertical ones (in the image shown in Fig. 4).

### 3.2 Experimental set-up

The drainage experiments are realized on an inverted microscope (Zeiss Axio Observer D1), using a wide-field sensitive camera Andor Zyla SCMos (frequency of acquisition on the order of 1 frame per second). A specific chip holder as well as a pressurization system have been developed owing to the high gas pressures (several tens of bars) required for the drainage experiment (details are presented in SI). The developed high-pressure gas supply line consists in connecting a bottle of gas pressurized with 200 bars to the chip holder. The fluid line includes a purge valve to rapidly decrease the pressure, a 3 nm filter and an in-house adapter for connecting the 1/4" BSP tubing (international standard for gas tubing) to microfluidic material. The line is connected to the bottle via a high-pressure stainless steel flexible tube. A pressure sensor (SETRA brand, Model 2016 / C216) is placed on the line downstream of the filter. The measurements are transmitted via an acquisition card (DAQ, National Instruments) and the reading and recording of the data are made under a LabView interface.

Experiments are carried out using de-ionized water as wetting fluid and nitrogen as non-wetting fluid. The fluid supply conditions of the nanofluidic chip are sketched in *Fig. 5a*. The inlet pressure of the injected fluid is increased step by step, by acting directly on the pressure regulator. Each step corresponds to an increase in pressure between 0.2 and 0.5 bar. We wait for the liquid and gas distribution in the device to be stabilized before increasing the gas pressure level again. The value is measured using the pressure sensor. The experiment is stopped once the breakthrough is reached, that is, when the injected gas exits at the network outlet. The variation of gas pressure applied in the experiment is depicted in *Fig. 5c*.

In order to analyze the experiments and perform their comparison with the numerical simulation, the drainage patterns are extracted by image processing using a code developed with Matlab ©, described in Appendix A.

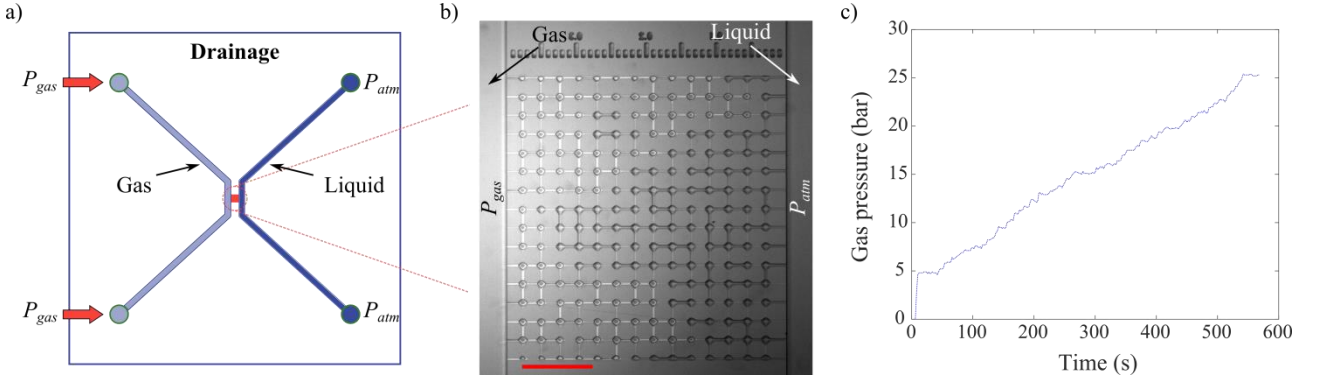


**Fig. 5** Illustration of drainage experiments in the nanofluidic system: a) The experiments are carried out by applying a gas pressure in one of the supply channels while maintaining the second one to atmospheric pressure  $P_{atm}$ ; b) Visualization of a drainage pattern during the experiment (gas phase in light gray, liquid phase in dark gray). The length scale (red bar) represents  $100 \mu\text{m}$ . c) Step by step pressure variation in the invading gas phase imposed in the experiment.

### 3.3 Numerical simulations

A test to analyze whether the drainage pattern is in agreement with Lenormand's diagram is to compare with a numerical simulation based on the classical invasion percolation algorithm (Wilkinson and Willemsen 1983). It is well established that this algorithm is adapted for describing the asymptotic regime dominated by capillarity, namely the capillary fingering regime. This algorithm can be summarized as follows. The network is invaded step by step starting from the inlet. Each step corresponds to the invasion of a single interfacial bond, namely a bond located at the interface between the two fluid phases. The pore occupied by the defending phase and adjacent to the invaded bond is also invaded. The interfacial bond invaded in a given step is the one having the lowest capillary pressure threshold along the gas–liquid interface. Using Laplace's law, the capillary pressure threshold of a bond is estimated as

$$p_c \approx \gamma \cos\theta \left( \frac{2}{w} + \frac{2}{h} \right) \approx \frac{2\gamma \cos\theta}{h} \quad (1)$$

where  $\gamma$  is the surface tension,  $\theta$  is the contact angle,  $h$  is the slit depth and  $w$  the slit width. Thus, the deeper the slit is, the lower its capillary pressure is. This simple invasion rule is combined with the trapping rule stating that a bond must be connected to the outlet through a path occupied by the defending fluid. Thus, the interfacial bonds of a trapped liquid cluster cannot be invaded. It is worth noting that the simulation is performed with a network having the same geometrical properties as the experimental one. In particular, the width and depth of each slit in the numerical network is the same as the corresponding slit in the experimental network (within the experimental accuracy margin of the fabrication process). Since the slit depth can take only six values in each direction, it can happen that several interfacial bonds can be invaded based on Eq.(1). When this is happening, one of those bonds is selected randomly. This can affect the order in which various regions of the network are invaded but tests have shown this has only a little impact on the final pattern (pattern at breakthrough). In order to perform a comparison with the pressure imposed in the experiment, an equivalent drainage pressure  $P_{drai}$  is associated with each numerical pattern. It is defined by,

$$P_{drai} = \max(p_{ci}, i = 1, n) + P_{atm} \quad (2)$$

where index  $i$  refers to the  $n$  bonds forming the invading phase cluster. Thus,  $P_{drai}$  is actually given by the capillary pressure threshold of the narrowest bond belonging to the gas cluster (to which the atmospheric pressure is added to obtain the gas pressure).

### 3.4 Results and discussions

A sequence of experimental binary images and a similar sequence obtained from simulation are presented in **Fig. 6**. As can be seen, the similarity between the experimental and numerical sequences is strong. It can also be observed that breakthrough at the network outlet takes place at a slightly different position in the simulation compared to the experiment. This can be explained by a slight difference between the experiment and the simulation concerning the size of the slits located in the breakthrough point area. This also explains the somewhat different breakthrough pressure observed in the experiment ( $P_{BT} \sim 20$  bars) and the one obtained in the simulation ( $P_{BT} \sim 15$  bars). However, the simulations for the other fabricated devices (not shown here) lead to the same breakthrough point as in the corresponding experiments.

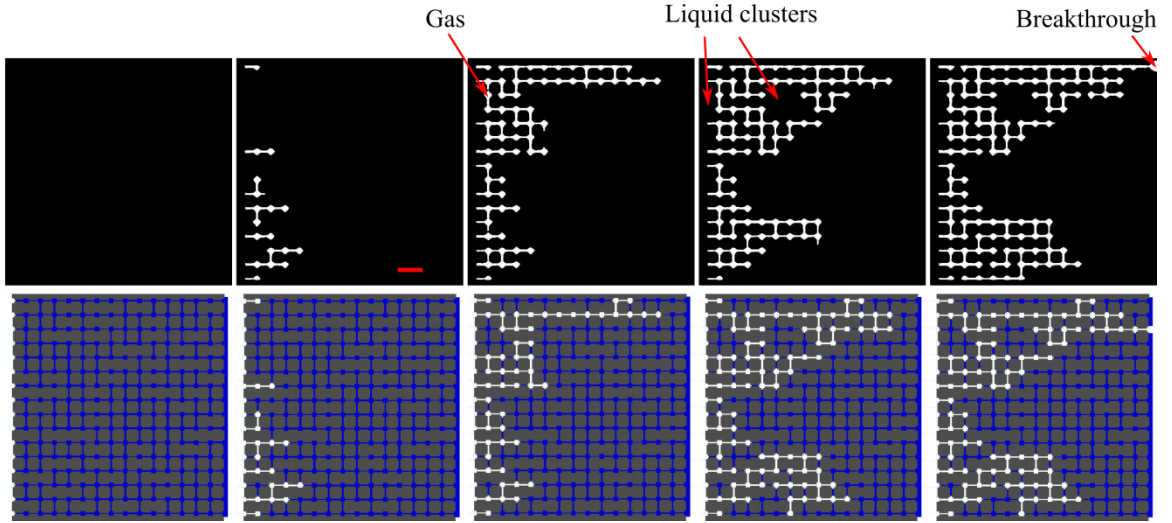


**Fig. 6** Top: drainage sequence in the experiment (gas phase in white, liquid phase in black). Two liquid clusters are indicated by arrows but several others, composed of one or two bonds, are present in the images. Bottom: a similar sequence obtained from numerical simulations.

The gas cluster forms a fingering structure. Isolated liquid clusters of various sizes can be also observed. The patterns strongly resemble the classical capillary fingering pattern of Lenormand's diagram. In our case, the viscosity ratio  $M$  is large, of the order of  $10^2$ , because the viscosity of the gas is lower than that of the liquid. On the other hand, the capillary number,  $Ca$ , is difficult to estimate simply because the invasion is driven by pressure step increment and not by imposing an injection flow rate. It tends to zero at the end of the displacement since we wait for the stabilization of the two phases between two pressure steps. The velocity of the fluids is therefore zero at the end of each pressure step.

A more quantitative comparison between the experiment and the simulation is presented in **Fig. 7**. The degree of similarity between the numerical and experimental patterns is first quantitatively determined using an indicator called the element matching indicator. To construct this indicator, the state (liquid or gas) of the same element (pore or bond) in the simulation and the experiment is

compared for the same drainage pressure. The element matching indicator between two patterns can be expressed as

$$EMI = \frac{1}{N} \sum_{i=1}^N I_i \quad (3)$$

where  $N$  is the number of elements in the network ( $N = \text{number of pores} + \text{number of bonds}$ );  $I_i$  is the matching indicator of element  $i$ :  $I_i = 1$  when the considered element is occupied by the same phase in both patterns whereas  $I_i = 0$  when this is not the case (liquid in pattern 1 and gas in pattern 2 or vice-versa). Thus,  $EMI = 1$  when the two patterns are perfectly identical whereas  $EMI = 0$  when none element is occupied by the same fluid in both patterns. The closer  $EMI$  to 1 is, the greater the degree of similarity between the two patterns is.

$EMI$  is plotted as a function of the pressure normalized by the experimental breakthrough pressure in **Fig. 7a**. As can be seen, indicator  $EMI$  is about 0.9 at the end of drainage. This indicates a fairly good agreement between the experimental and numerical drainage patterns. The value of the total indicator decreases to a minimum value of about 0.8 during drainage. This value is explained by a slight offset of the drainage pressure for some elements between the simulation and the experiment, meaning that some elements are drained in the simulation for a lower pressure level than in the experiment.

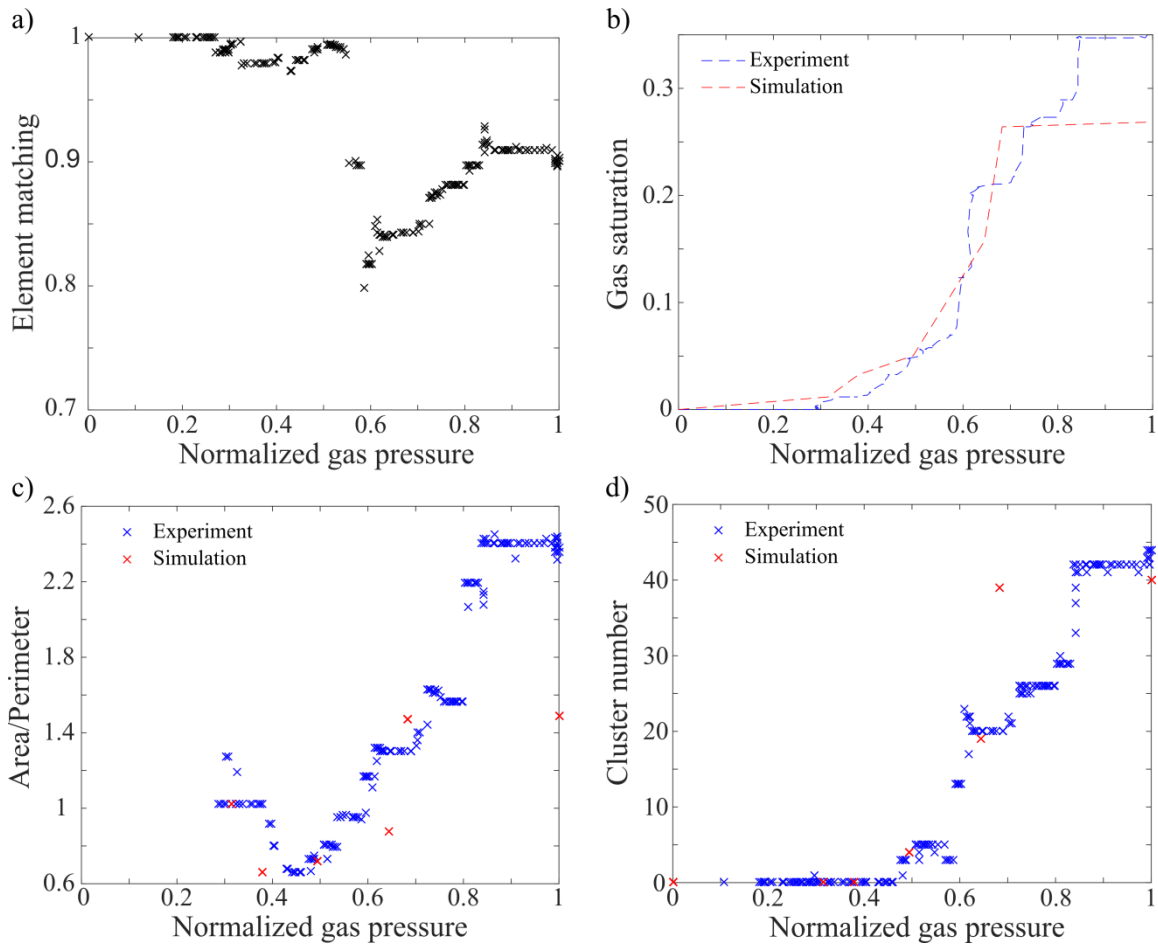


**Fig. 7** Comparison between experiment and simulation. The pressure is normalized by the breakthrough pressure  $P_{BT}$  ( $P_{BT} \sim 20$  bars in the experiment and  $P_{BT} \sim 15$  bars in the simulation)

As discussed for instance in (Mecke 1996), various other indicators can be defined to quantitatively compare patterns. *Fig. 7b* shows the gas saturation (ratio of the element numbers occupied by the gas phase to the total element numbers in the network) whereas *Fig. 7c* shows the variation of the ratio of the gas area to its perimeter. The latter corresponds to the exterior perimeter of the invasion pattern and the former is defined as the area of the surface delimited by the exterior perimeter. This indicator is related to the global shape of the meniscus (a flat, isotropic drainage leads to a high area/perimeter value whereas fingers have a large perimeter englobing a low area). Finally, *Fig. 7d* shows the number of liquid clusters in the system as a function of normalized gas pressure. As can be seen, the agreement between the experimental and numerical patterns is quite good for all considered indicators. However, it can be observed that more isolated clusters forms in the numerical computation compared to the experiment when the normalized gas pressure is around 0.7. Moreover, there are as many clusters at the end whereas the gas saturation is lower in computation. That means the density of isolated clusters is higher in the computation. This is because the invasion of the pores takes place sequentially in the simulation, one after the other. In the experiment, several pores can be drained at the same time. This is an indication that the experiment does not fully correspond to a pure capillary fingering regime. This reduces the probability of isolated cluster formation. Moreover, it is known that the slit shape (width much larger than depth) favors the formation of thick liquid film along the lateral edges of the slits invaded by the gas phase when the top and bottom walls are not perfectly parallel, e.g. (Geoffroy et al. 2006; Keita et al. 2016). Those films interconnect the different slits and pores together, offering liquid paths for the “isolated” liquid clusters to be drained in the experiments.

The conclusion is therefore that the slow drainage process in the nanofluidic network with bond depths varying between 0 and 225 nm is not markedly different from the process observed and analyzed in previous works in model systems with much larger bond sizes. Also, the good agreement between the experiment and the simulation indicates that the dominant drainage mechanisms at the pore scale are piston-like motions and Haines jump since they are the mechanisms taken into account in the invasion percolation algorithm, albeit rather approximately as regards the Haines jump. As mentioned above thick liquid films are present in the slits invaded by the gas phase but the presence of corner films is also classical in systems with pores of greater size, e.g. (Blunt et al. 2002).

#### 4. Conclusion

We presented a grayscale laser direct writing lithography (GLDWL) method to design structures in 2.5 dimensions in positive photoresist with nanometer depth resolution. We achieved the fabrication of a network of interconnected slits with depths in the range 0 - 225 nm. Lateral resolution depends directly on the laser beam diameter and is around 2  $\mu\text{m}$  in this study. Etching is optimized to reach selectivity around 1 in order to transfer the resist structure into silicon without geometrical distortion. A visual control of the remaining resist thickness based on white light interference enables checking the result of the lithography in a large area at a glance. This technique can be easily incorporated in a standard process flow chart. This study is done optimizing the bake process of a positive photoresist initially developed for binary lithography to adapt it to GLDWL.

presents the versatility of a maskless technique which is convenient for the prototyping phase. But at the same time, it does not necessitate the very long writing time of other direct writing methods with nanometer resolution as e-beam. In case of large structures, it is also feasible to save writing time with a larger beam diameter. This technique suits very well the needs of nanofluidics; nanometric complex depth profiles (in order to control confinement) and micrometer lateral dimension (to have a high throughput in lab-on-chip application, and to work under an optical microscope). This is of high relevance for two-phase flows in nanoporous media, since depth controls capillary pressure that in turn controls flow properties. Thus, GLDWL opens the way to further study on nano-confined fluid, liquid under tension or two-phase flow phenomena. More generally, nanofluidic complex topologies accessible with a simple process have great potential in lab-on-chips, to implement functions such as DNA concentration (Ranchon et al. 2016), or fluidic diodes (Vlassioux and Siwy 2007). The approach can also be easily adapted to other application fields (optics, MEMS).

The development of GLDWL nanofluidic devices was primarily motivated by the analysis of immiscible two-phase flow in nanoporous materials, an important class of porous media. The aim was to assess whether the drainage process in nanoporous systems is significantly different from what is known in micrometric systems. Our results indicate that the slow drainage process in nanoporous systems well corresponds to the capillary fingering regime in Lenormand's diagram, and thus can be analyzed within the framework of invasion percolation theory, quite similarly as in micrometric systems. However, it would be worthwhile to pursue the study for higher capillary numbers, so to verify the whole Lenormand's diagram. This would necessitate developing another fluid delivering system to maintain a constant gas flow at high pressure. The fact that the drainage process is not fundamentally different in our nanofluidic device does not mean this also holds for other two-phase flow processes, such as for instance evaporation and imbibition since, as mentioned in the introduction, previous works indicate differences with the behaviors in the micrometric systems.

The situation could also be different in systems involving still smaller pores on the order of 1 nm or less where the classical continuum laws cease to be good approximations, e.g. (Falk et al. 2015). Also, local deformation was negligible in our experiment. Owing to the high capillary pressures induced by the submicronic sizes, coupling between flow and deformation of the pore space are more likely to occur in nanoporous systems than in micrometric systems (for similar mechanical properties of the solid matrix). This can have a great impact on the drainage patterns when the deformability of the medium is sufficiently high, (Holtzman and Juanes 2010).

## 5. Acknowledgements

This work was partly supported by LAAS-CNRS micro and nano technologies platform member of the French RENATECH network. It was also supported by LEAF Equipex project. Authors thank also Andra, INSIS-CNRS institute, and NEEDS-MIPOR CNRS program for the financial support. We acknowledge P. Dubreuil and A. Lecestre for help with the etching parameters, B. Reig for AFM imaging and J. Prautzsch for help in the pore network simulations.

## 6. References

Azimi S, Dang Z, Zhang C, et al (2014) Buried centimeter-long micro- and nanochannel arrays in porous silicon and glass. *Lab Chip* 14:2081–2089. doi: 10.1039/c4lc00062e

- Blunt MJ, Jackson MD, Piri M, Valvatne PH (2002) Detailed physics, predictive capabilities and macroscopic consequences for pore-network models of multiphase flow. *Adv. Water Resour* 25:1069–89.
- Chauvet F, Geoffroy S, Hamoumi A, et al (2012) Roles of gas in capillary filling of nanoslits. *Soft Matter* 8:10738–10749. doi: 10.1039/c2sm25982f
- Cottin C, Bodiguel H, Colin A (2010) Drainage in two-dimensional porous media: From capillary fingering to viscous flow. *Phys Rev E - Stat Nonlinear, Soft Matter Phys* 82:1–10. doi: 10.1103/PhysRevE.82.046315
- Duan C, Karnik R, Lu M-C, Majumdar A (2012) Evaporation-induced cavitation in nanofluidic channels. *Proc Natl Acad Sci U S A* 109:3688–93. doi: 10.1073/pnas.1014075109
- Duan C, Majumdar A (2010) Anomalous ion transport in 2-nm hydrophilic nanochannels. *Nat Nanotechnol* 5:848–852. doi: 10.1038/nnano.2010.233
- Duan C, Wang W, Xie Q (2013) Review article: Fabrication of nanofluidic devices. *Biomicrofluidics* 7:26501. doi: 10.1063/1.4794973
- Dullien FAL (1992) *Porous Media, Fluid Transport and Pore structure*.
- Erdmanis M, Tittonen I (2014) Focused ion beam high resolution grayscale lithography for silicon-based nanostructures. *Appl Phys Lett*. doi: 10.1063/1.4866586
- Falk K, Coasne B, Pellenq R, et al (2015) Subcontinuum mass transport of condensed hydrocarbons in nanoporous media. *Nat Commun* 6:6949. doi: 10.1038/ncomms7949
- Gale MT, Rossi M, Pedersen J, Schulz H (1994) Fabrication of Continuous-Relief Micro-Optical Elements By Direct Laser Writing in Photoresists. *Opt Eng* 33:3556–3566.
- Geoffroy S, Plouraboué F, Prat M, Amyot O (2006) Quasi-static liquid-air drainage in narrow channels with variations in the gap. *J Colloid Interface Sci* 294:165–175. doi: 10.1016/j.jcis.2005.07.008
- He K, Xu L, Gao Y, et al (2015) Evaluation of surfactant performance in fracturing fluids for enhanced well productivity in unconventional reservoirs using Rock-on-a-Chip approach. *J Pet Sci Eng* 135:531–541. doi: 10.1016/j.petrol.2015.10.008
- Holtzman R, Juanes R (2010) Crossover from fingering to fracturing in deformable disordered media. *Phys Rev E* 82:046305. doi: 10.1103/PhysRevE.82.046305
- Jung M, Brinkmann M, Seemann R, et al (2016) Wettability controls slow immiscible displacement through local interfacial instabilities. *Phys Rev Fluids* 074202:1–19. doi: 10.1103/PhysRevFluids.1.074202
- Ke K, Hasselbrink EF, Hunt AJ (2005) Rapidly prototyped three-dimensional nanofluidic channel networks in glass substrates. *Anal Chem* 77:5083–5088. doi: 10.1021/ac0505167
- Keita E, Koehler SA, Faure P, et al (2016) Drying kinetics driven by the shape of the air/water interface in a capillary channel. *Eur Phys J E* 39:23. doi: 10.1140/epje/i2016-16023-8
- Kim J, Joy D-C, Lee S-Y (2007) Controlling resist thickness and etch depth for fabrication of 3D structures in electron-beam grayscale lithography. *Microelectron Eng* 84:2859–2864. doi: 10.1016/j.mee.2007.02.015

- Lee H, Lee SG, Doyle PS (2015) Photopatterned oil-reservoir micromodels with tailored wetting properties. *R Soc Chem* 15:3047–55. doi: 10.1039/c5lc00277j
- Lenormand P, Touboul E, Zarcone C (1988) Numerical models and experiments on immiscible displacements in porous media. *J Fluid Mech* 189:165–187.
- Li L, Gattass RR, Gershgoren E, et al (2009) Achieving 1/20 Resolution by One Color Initiation and Deactivation of Polymerization. *Science* (80- ) 324:910–913.
- Liao Y, Cheng Y, Liu C, et al (2013) Direct laser writing of sub-50 nm nanofluidic channels buried in glass for three-dimensional micro-nanofluidic integration. *Lab Chip* 13:1626–1631. doi: 10.1039/c3lc41171k
- Lin C, Sullivan RF (1972) An Application of White Light Interferometry in Thin Film Measurements. *IBM J Res Dev* 16:269–276. doi: 10.1147/rd.163.0269
- Madou MJ (2011) *Fundamentals of Microfabrication and Nanotechnology*, Third edit. CRC Press
- Mecke K (1996) Morphological characterization of patterns in reaction-diffusion systems. *Phys Rev E* 53:4794–4800. doi: 10.1103/PhysRevE.53.4794
- MicroChemicals GmbH (2013) *Greyscale Lithography with Photoresists*.
- Naillon A (2016) *Ecoulements liquide-gaz, évaporation, cristallisation dans les milieux poreux et nanoporeux. Etudes à partir de systèmes micro et nanofluidique*. University of Toulouse
- Prat M (2002) Recent advances in pore-scale models for drying of porous media. *Chem Eng J* 86:153–164. doi: 10.1016/S1385-8947(01)00283-2
- Rammohan A, Dwivedi PK, Martinez-Duarte R, et al (2011) One-step maskless grayscale lithography for the fabrication of 3-dimensional structures in SU-8. *Sensors Actuators B Chem* 153:125–134. doi: 10.1016/j.snb.2010.10.021
- Ranchon H, Malbec R, Picot V, et al (2016) DNA separation and enrichment using electrohydrodynamic bidirectional flows in viscoelastic liquids. *Lab Chip* 16:1243–1253. doi: 10.1039/C5LC01465D
- Selimis A, Mironov V, Farsari M (2015) *Microelectronic Engineering Direct laser writing: Principles and materials for scaffold 3D printing*. *Microelectron Eng* 132:83–89. doi: 10.1016/j.mee.2014.10.001
- Shih W-P (2004) Collapse of microchannels during anodic bonding: Theory and experiments. *J Appl Phys* 95:2800. doi: 10.1063/1.1644898
- Stavis SM, Geist J, Gaitan M, et al (2012) DNA molecules descending a nanofluidic staircase by entropophoresis. *Lab Chip* 12:1174–1182. doi: 10.1039/c2lc21152a
- Stavis SM, Geist J, Gaitan M (2010) Separation and metrology of nanoparticles by nanofluidic size exclusion. *Lab Chip* 10:2618–2621. doi: 10.1039/c0lc00029a
- Stavis SM, Strychalski E a, Gaitan M (2009) Nanofluidic structures with complex three-dimensional surfaces. *Nanotechnology* 20:165302. doi: 10.1088/0957-4484/20/16/165302
- Sugioka K, Cheng Y (2014) Femtosecond laser three-dimensional micro- and nanofabrication. *Appl Phys Rev* 1:041303. doi: 10.1063/1.4904320
- Totsu K, Fujishiro K, Tanaka S, Esashi M (2006) Fabrication of three-dimensional microstructure

using maskless gray-scale lithography. *Sensors Actuators A Phys* 130-131:387–392. doi: 10.1016/j.sna.2005.12.008

Vincent O, Szenicer A, Stroock AD (2016) Capillarity-Driven Flows at the Continuum Limit. *Soft Matter* 12:6656–6661. doi: 10.1063/1.2829813

Vlassioug I, Siwy ZS (2007) Nanofluidic diode. *Nano Lett* 7:552–556. doi: 10.1021/nl062924b

Washburn EW (1921) The dynamics of capillary flow. *Phys Rev* 17:273 – 283.

Wilkinson D, Willemsen JF (1983) Invasion percolation: a new form of percolation theory. *J Phys A Math Gen* 16:3365–3376. doi: 10.1088/0305-4470/16/14/028

Witten TA, Sander LM (1981) Diffusion-Limited Aggregation, a Kinetic Critical Phenomenon. *Phys Rev Lett* 47:1400–1403.

Wu MH, Park C, Whitesides GM (2002) Fabrication of arrays of microlenses with controlled profiles using gray-scale microlens projection photolithography. *Langmuir* 18:9312–9318. doi: 10.1021/la015735b

Wu Q, Bai B, Ma Y, et al (2014), Optic imaging of two-phase flow behavior in 1D nanoscale channels, *SPE Journal* 19 (05), 793-802.

Zhang C, Oostrom M, Wietsma TW, et al (2011) Influence of viscous and capillary forces on immiscible fluid displacement: Pore-scale experimental study in a water-wet micromodel demonstrating viscous and capillary fingering. *Energy and Fuels* 25:3493–3505. doi: 10.1021/ef101732k

Zhang J, Guo C, Zhang H, Liu Q (2013) One-step fabrication of micro/nanotunnels in metal interlayers. *Nanoscale* 5:8351–8354. doi: 10.1039/c3nr01677c

Zhong K, Gao Y, Li F, et al (2014) Fabrication of PDMS microlens array by digital maskless grayscale lithography and replica molding technique. *Optik (Stuttg)* 125:2413–2416. doi: 10.1016/j.ijleo.2013.10.082

## Appendix A : Drainage pattern image processing

In order to analyze the experiments and perform the comparison between the experiment and the numerical simulation, the drainage patterns are extracted by image processing using a code developed with Matlab ©. The purpose of this code is to determine the drained pores and bonds. The various processing steps can be summarized as follows and illustrated in figure A1 (one can refer to (Naillon 2016) for more details). A background image is opened in step 1. It compensates for defects in the homogeneity of illumination and eliminates dust that may be present on the lens or sensor of the camera. From this image a matrix E is created, which measures the difference in gray level (luminous intensity) between a pixel and the average value of the gray level in the image. Step 2 corresponds to the opening of the sequence of images using the LibTiff library of Matlab ©. This library provides functions that are optimized to reduce the opening time of an image stack in .tif format (image sequence into a single file). The matrix E is subtracted from all the images in step 3 in order to correct the illumination defects. Then, a reference image is extracted from the image sequence in step 4. It corresponds to the mean value of all the images before the drainage begins (typically the average of more than a dozen images). In step 5, the reference image is subtracted from all images. In devices with variable depths, the passage of gas can indifferently increase or decrease the gray level of a channel along its depth. We therefore calculate the absolute value of the difference. We then get an image on which black areas correspond to areas where nothing has happened, and clear areas to areas where there has been a change. The next step is to convert the grayscale image from step 5 to binary image. This leads to a black and white image that clearly distinguishes where a change has occurred (gas invasion) from where there has been no change. The threshold is first detected automatically on an image with the threshold function based on the Otsu method. The latter allows minimizing the interclass variance of the white and black pixels. The black and white image is obtained in step 6. The program is intended to be interactive and the user can manually modify the threshold after observing the result. In general, a threshold lower than the one proposed automatically by Matlab is chosen manually even if this leads to a lot of background noises. The objective is to avoid not taking into account drained areas. The image is cleaned in step 7 by eliminating all pixel clusters composed of a number of pixels smaller than a number chosen by the user. Typically, a threshold of 200 pixels (which corresponds to a surface area of about  $4.5 \times 4.5 \mu\text{m}^2$ ) is sufficient to remove the isolated clusters without removing drained areas. Finally, the dilation and erosion functions are used to eliminate the "holes" of black pixels in the middle of the drained zones. In particular, we realized that the conversion process in black and white image had difficulty detecting the gray level variations at the center of the pores. In the same way as for step 6, the user can modify the parameters of steps 7 to 9 interactively by directly controlling the result. The parameters that were used for steps 6 and 9 are then used to process the entire image sequence in the same manner. The last step (10) consists in detecting the state of each pore and bond, drained or not. To this end, we take the median value of the pixels of a window placed in the middle of each pore and bond. If the median value in this window is equal to 1 (white pixel), we consider the pore or the bond as drained. If it is 0, we consider that it has not been drained. For some acquisitions, we observed that some images had a higher average luminous intensity. We think that this phenomenon comes from a poor control of the exposure time of the camera that we had set as low as possible (10 ms). In this case, we added an additional step between steps 3 and 4 to compensate for temporal variations in mean gray levels of the images.

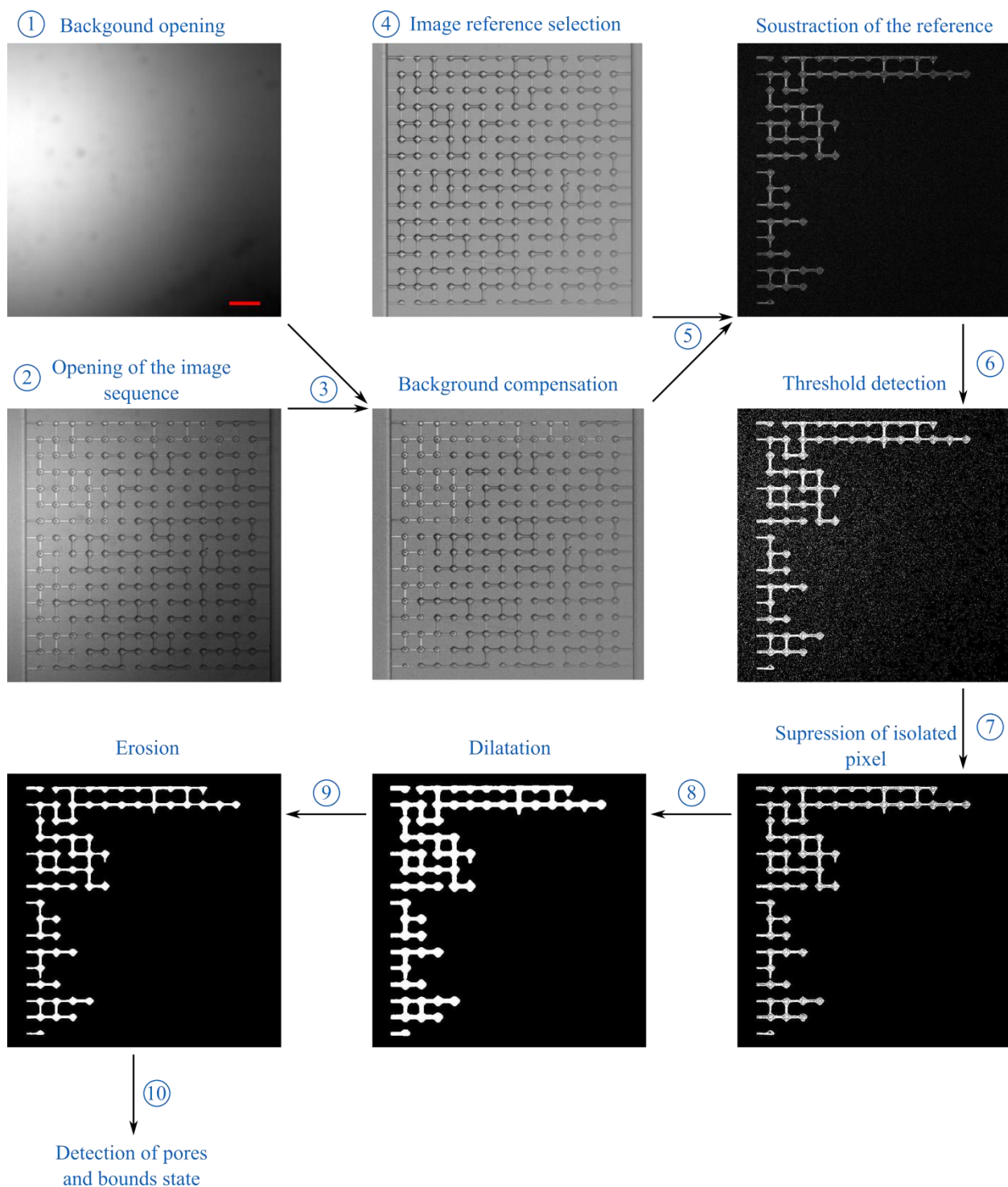
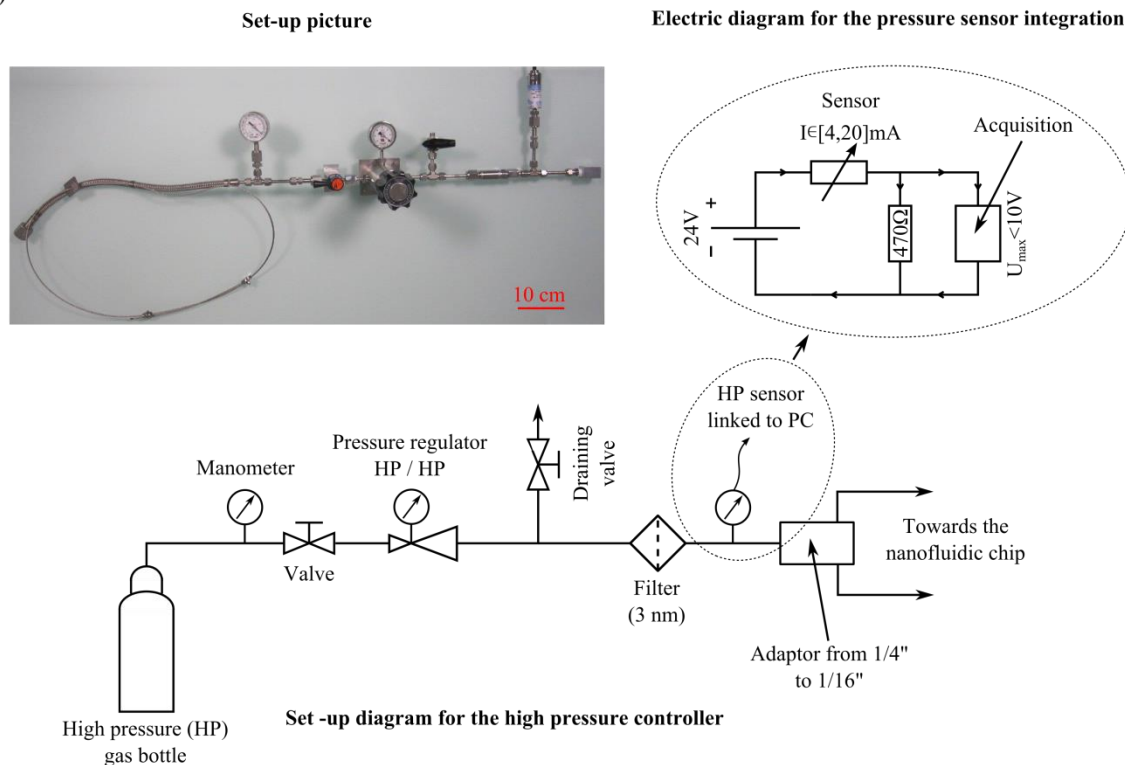


**Fig. A1**– Illustration of drainage pattern image processing extraction algorithm. Each image is represented with their full scale of gray level to facilitate observation. To this end, the contrast is increased to get a representation between white and black on all images. The change in contrast is therefore different from one image to another. For example, for the background image, this representation may wrongly suggest that the inhomogeneity in illumination is quite large. The length scale (red bar) represents 50 µm.

## SI 1. Experimental bench: in-house high pressure controller and nanochip holder.

a)



b)

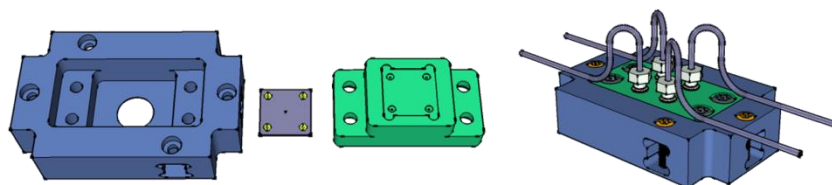


**Fig SI.1** a) High pressure gas supply line for drainage experiments and diagram of the integration of the high pressure sensor. b) CAD picture of the chip holder developed to supply a high pressure to the nanofluidic chip. The chip is maintained between the stainless steel base (blue) and the PEAK top cover (green). Fluid is supplied from tubes connected to the cover thanks to coned fittings. Fluid leaks are avoided using O-rings.

## SI 2. Optimization of the 2.5 grayscale laser direct writing (GLDW) process

### SI 2a. Influence of the interline distance between two laser passages on surface homogeneity

As explained in section 2.2, at the sight of the lateral resolution we target, it is decided to use a laser beam focused in a  $2 \mu\text{m}$  diameter. To ensure a homogeneous exposure dose on the entire surface while keeping a low writing time, we study the influence of the interline distance between two laser

passages. Experiments are done and compared with calculations taking into account the Gaussian profile of the laser beam. The representation of a Gaussian beam is presented in **Fig SI.1**.

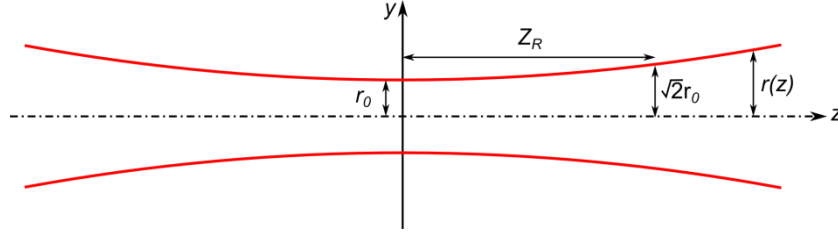


**Fig SI.1:** Gaussian beam with the presentation of its key geometrical parameters: the waist,  $r_0$ , and the Rayleigh length,  $Z_R$ .

For a Gaussian beam, the radius  $r$  evolves with the distance  $z$  to the focus point as:

$$r(z) = r_0 \sqrt{1 + \left(\frac{z}{Z_R}\right)^2}, \quad (\text{SI1})$$

where  $r_0$  is the beam diameter at the origin (focused point) and it is called the waist.  $Z_R$  is the Rayleigh distance for which the radius is  $\sqrt{2}$  times higher than  $r_0$  (the surface is multiplied by 2).  $Z_R$  is related to  $r_0$  as:

$$Z_R = \frac{\pi r_0^2}{\lambda}, \quad (\text{SI2})$$

with  $\lambda$ , the wavelength of the laser. At last, the density of light energy  $I$  evolves with  $y$  and  $z$  as:

$$I(y, z) = I_0(z) e^{\frac{-2y^2}{r(z)^2}} \quad (\text{SI3})$$

where  $I_0$  is the density of light energy for  $y=z=0$ . With this expression, we compute the light energy which is received by a surface swept by a beam at a known velocity. Experimentally, 3 rectangles of  $100 \times 50 \mu\text{m}^2$  are written with successive beam passages in the longitudinal direction. The interline distance,  $i$ , is respectively 1, 2 and  $3 \mu\text{m}$  for a writing velocity of 1.2, 0.6 and  $0.4 \text{ mm/s}$ . In this way, the amount of the incident light energy on the surface is the same in all cases. Result of the lithography is shown in **Fig SI.2a**. Beam passages are observed for an interline distance greater than 1. AFM measurements are done in the transversal direction (represented by the dotted line in **Fig SI.2a**) to evaluate the depth of the non-homogeneities on the surface (presented in **Fig SI.2b**). The theoretical exposure dose is computed using expressions above, it is plotted in **Fig SI.2c**. It appears that the shape profile of the surface corresponds accurately to the shape of the exposure dose. When the interline distance is higher than  $1 \mu\text{m}$ , exposure dose is not homogeneous on the surface and causes variations of the resist development rate. Theoretically, an interline distance lower than  $1 \mu\text{m}$  would give a more homogeneous surface, but the writing time would increase unless the writing velocity is increased. Unfortunately, some defects on the surface are observed in

**Fig SI.2a** for writing velocity of 1.2mm/s. We have observed that the higher the velocity is, the bigger the defects are. That is why writing velocity is kept at 0.4 mm/s for the optimized process.

In **Fig SI.2d**, the impact of the focusing is shown. For each line, the focus lens is moved 20 $\mu$ m. The focus point is between the second and the third line. It is shown that the unfocusing allows increasing the beam diameter by reducing its surface power. Thus, this trick can be used to homogenize the exposure dose on the surface if a good lateral resolution is not needed.

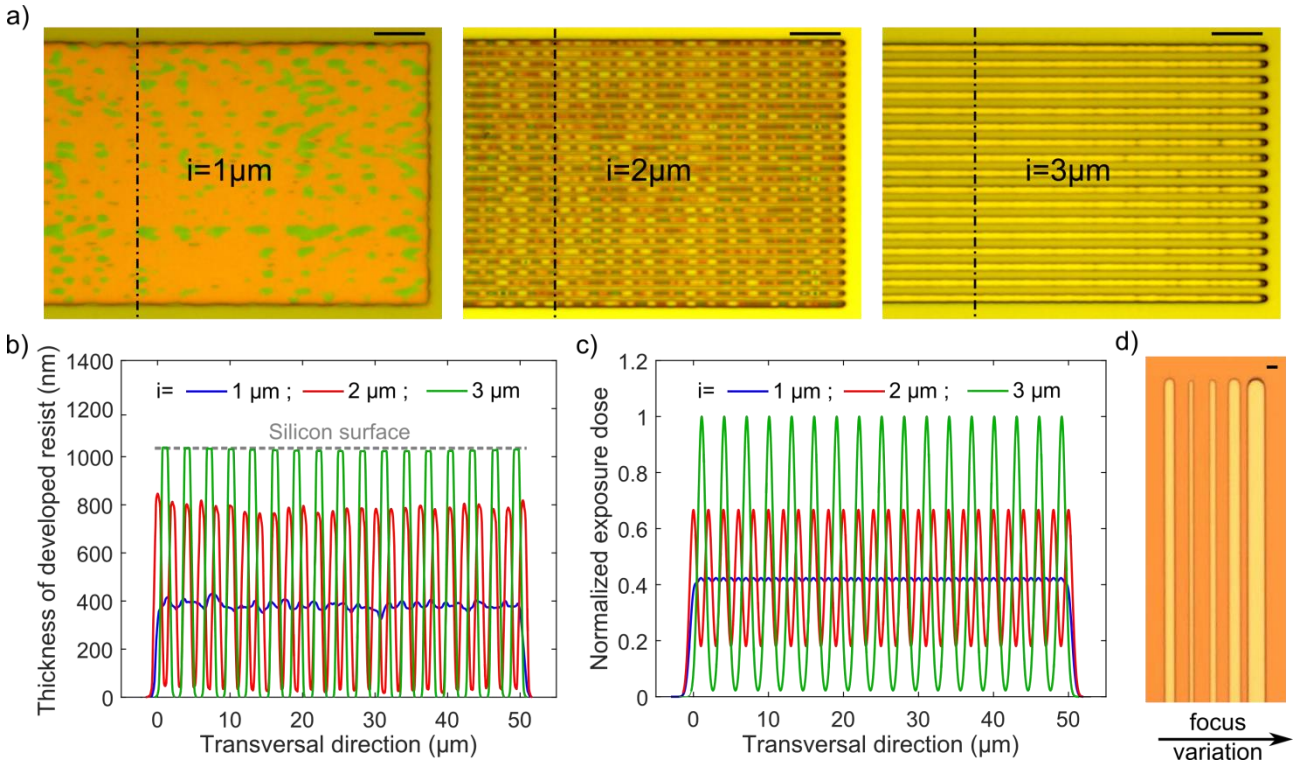


**Fig SI.2:** Influence of the interline distance,  $i$ , between two laser passages and influence of the focalization of beam. a) Rectangle of partially developed resist drawn with  $i$  from 1 $\mu\text{m}$  (left) to 3 $\mu\text{m}$  (right). b) and c): Respectively the experimental measured depth and the local exposure dose in the transversal direction of writing for  $i$  equal 1, 2 and 3 $\mu\text{m}$ . d) Influence of the beam focus on the beam diameter. For each line, the objective is moved 20 $\mu\text{m}$ . The focus is between the second and third line.

### SI 2b. Optimization of the etching process to have a selectivity of 1.

For our process, it is interesting to develop an etching recipe with a low selectivity around 1 ( $S = v_{Si,e}/v_{r,e}$ ). In this way, the nanostructures patterned in the resist are identically transferred into the silicon. This specification is unconventional for binary process for which the etching recipes are developed to have the highest selectivity as possible. Indeed, a high selectivity allows etching deep tranches with a thin layer of resist ensuring a good lateral resolution.

We modified a recipe used in binary process with  $S \sim 7$  to decrease its selectivity. The process is optimized for a reactive ion etching machine (Alcatel AMS4200, inductively coupled plasma, ICP RIE). Etching is done by plasmas of  $\text{SF}_6$ ,  $\text{C}_4\text{F}_8$  and  $\text{O}_2$ . Reactive ion etching couples chemical and

physical etching. The chemical part of the etching is controlled by the ionized gas concentration; mainly SF<sub>6</sub> for silicon etching and O<sub>2</sub> for the resist etching (C<sub>4</sub>F<sub>8</sub> is used for surface passivation). These concentrations depend on the input gas flow and on the power of the magnetic field for ionization (P<sub>ICP</sub>). The physical part of the etching corresponds to the ion bombardment on the surface and it is controlled by the bias power, P<sub>bias</sub>.

Thus, in order to reduce the selectivity, we implemented a recipe which favors physical etching, and with a lower SF<sub>6</sub> concentration and a higher O<sub>2</sub> concentration than the one used for binary process. The selected parameters are the following; gas flow: SF<sub>6</sub>:15 sccm, O<sub>2</sub>:10 sccm and C<sub>4</sub>F<sub>8</sub> sccm, P<sub>bias</sub>=90W, P<sub>ICP</sub>=450W and the pressure is set to 5.10<sup>-3</sup> mbar. We obtain a selectivity of 0.93 and  $v_{Si,e}=270$  nm/min.